Two-level Design Optimization of AC Machines with DC Stator Excitation and Minimal Torque Ripple using Reluctance Rotor Profile Shaping

Ali Mohammadi, Oluwaseun A. Badewa, Yaser Chulaee, and Dan M. Ionel
SPARK Laboratory, Stanley and Karen Pigman College of Engineering, University of Kentucky, Lexington, KY, USA
alimohammadi@uky.edu, o.badewa@uky.edu, yaser.chulaee@uky.edu, and dan.ionel@ieee.org

***Abstract*—Torque ripple mitigation in electric machines is important for a smooth and stable operation, minimize mechanical vibrations, and enhance the overall performance. In this paper, a novel two-level optimization method is proposed for the design of synchronous flux-switching and hybrid excitation machines with an innovative multi-point spline shaping method to minimize the torque ripple. This study uses models that are validated by experimental tests from a prototype with similar topology, and exemplifies the aforementioned optimization process on a 28 pole machine. The analysis results indicate that the torque ripple can be substantially reduced with improved electromagnetic torque of the electric machine, and the combination of force analysis and the multi-point spline shaping ensure the manufacturability of the machine.**

***Index Terms*—Synchronous machine, flux switching, flux reversal, hybrid excitation, reluctance rotor, rotor teeth profile, optimization, minimal torque ripple, spline shaping.**

I. Introduction

The continuous advancement of technology in electric machines is crucial for improving performance and maintaining competitiveness [1]. This persistent innovation is necessary to drive progress and meet the increasing demands of the dynamic electric machine industry, which is pivotal in sectors such as transportation, energy generation, and industrial automation [2], [3].

Reluctance rotor machines exhibit robustness suited for high-speed operation and stator-only cooling solutions, as the losses are primarily confined to the stator. Electric motors, which employ concentrated winding in the stator with reluctance rotors are of different varieties, such as those typically labeled as flux switching, flux reversal, and hybrid-excited synchronous machines [4]–[7]

In the machine under study, the stator consists of a wound DC excitation and toroidally wound coils for armature phase winding. The stator core features rectangular slots that facilitate the use of rectangular wire, resulting in a high slot fill factor and minimal copper losses. The toroidally wound concentrated coils have compact axial ends, which further reduces the copper losses [8]–[10].

The winding pattern follows the three-phase succession around the stator circumference, and only one coil side in each slot ensures high fault tolerance [11]. The PMs are radially positioned in the stator, with each pair magnetized tangentially in opposite directions. The rotor, which lacks active excitation components, comprises a laminated steel core of the reluctance type with protrusions, whose number and dimensions are coordinated with the stator characteristics [12]–[14].

It is crucial for electric motors to operate with minimal noise and vibration to ensure an overall reliable and consistent performance [15]–[17]. An inherent and undesirable characteristic encountered in electric motors is represented by the torque ripple [18]. The primary contributors to torque ripple include non-ideal back-EMF waveform, saturation in the machine's magnetic circuit, and cogging torque. Cogging torque arises due to the attraction between the rotor poles and the stator teeth [19], [20]. The rotor rotation and change in its alignment with respect to the stator, leads to variations in reluctance, resulting in periodic changes of instantaneous torque [21]–[23].

The effect of reluctance variation is more pronounced at low speeds, with inertia playing a role in mitigating cogging torque at higher speeds [24], [25]. Other causes of torque ripple, may include for example saturation that modifies the airgap flux density [26], [27]. Different methods to mitigate torque ripple have been extensively investigated. For instance, magnet shaping has been analyzed as a solution for torque ripple reduction in a 24/8 slot/pole machine [27].

Similarly, designing an asymmetric rotor shape in a 12/8 slot/pole electric machine has been shown to reduce torque ripple by 40% at the cost of a 5% reduction in machine torque [28]. The use of a mirror asymmetric rotor to reduce torque ripple has also been explored [26]. Torque ripple in axial flux coaxial magnetic gears and pole pair selection has been examined [21], and alternate rotor geometry in a switched reluctance machine has shown reduced torque ripple [23].

The electric machine in this paper operates as a synchronous machine, hence, it is expected that profiling the rotor would reduce the torque ripple as it is systematically shown in the paper. Torque ripple reduction in a flux-switching machine with a 12/10 slot/pole combination has been reported, utilizing short magnets and stator flux bridges [29]. Magnet shifting in a 48/8 slot/pole machine achieved a 28% torque ripple reduction [30]. Furthermore, a staggered rotor design in a 9/6 slot/pole machine reduced torque ripple by 60% [31], and optimization of slot, teeth, and magnet sizes in a 48/8 slot/pole machine resulted in a 58% reduction in torque ripple [32].

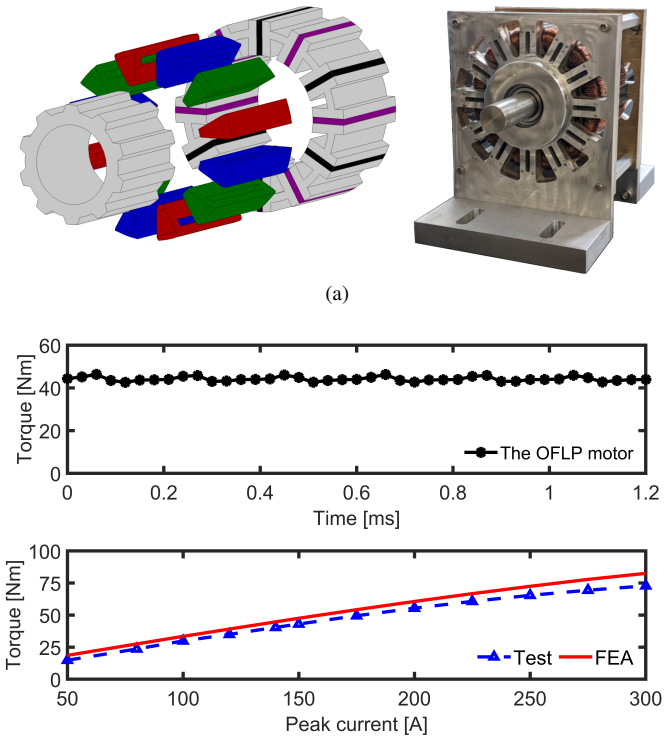

(a)

(b)

Fig. 1. (a) Exploded view of the PM stator excitation design on the left and the full assembly of the open frame lab prototype (OFLP) on the right. (b) Example validation of computational models versus experimental results.

II. Machine Topology and Reference Prototype

This paper studies motors that are part of a general class of synchronous machines including those that may have been referenced in recent literature as of the flux switching, variable flux reluctance, or hybrid excitation type [18], [29]. The target design for optimization has the same type of rotor and operating principle as the prototype depicted in Fig. 1(a), which in this paper serves as a calibrated model for validation [9]. The torque and torque ripple of the prototype have been previously validated by experimental tests and finite element analysis (FEA) as shown in Fig. 1(b).

The configuration of the electric machine under study as depicted in Fig. 2, has 24 stator teeth and 14 rotor protrusions. In this configuration, compared to the prototype, the PMs are replaced by one winding, which has the coil sides optimally placed in the stator core and is supplied by a controlled DC voltage source to produce the excitation field in combination with the moving reluctance consequent pole rotor. The design with DC stator excitation is of specific interest for rotor profile shaping because the torque ripple varies depending on the excitation and is influenced by the saturation, whereas, in the design with PMs, the excitation field is constant.

The half-symmetry computation domain of the DC-excited stator design is shown by the flux density distribution map in Fig. 2. This design utilizes stator serpentine DC winding and concentrated AC coils toroidally wound around the back iron, resulting in a high winding factor. The stator core features

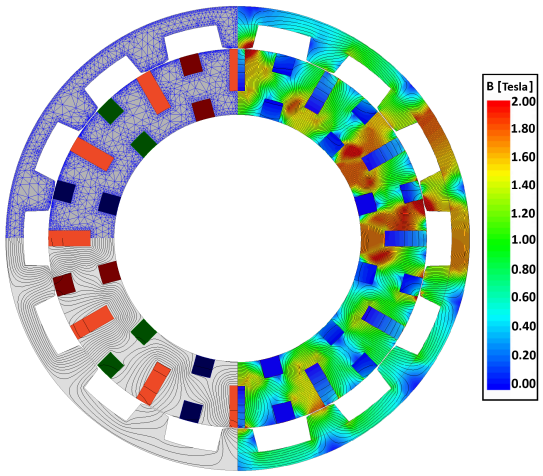

Fig. 2. Cross-sectional view of the design with serpentine DC stator excitation, toroidally wound AC windings, and profiled rotor, showing the detailed mesh, flux lines, and flux-density distribution. The flux-density is depicted on the computational domain of the design.

rectangular slots that allow for the use of rectangular wire, resulting in a high slot fill factor and reduced copper losses.

The serpentine DC winding, along with the AC concentrated toroidal coils with compact axial ends, significantly helps in minimizing copper losses. To show the operating principle and torque production mechanism, the open-circuit (OC) DC winding and OC armature fields should be analyzed based on the MMF-permeance model. The electromagnetic torque using airgap flux density distributions of DC winding, $B_{DC}(\varphi,t)$, and armature winding, $B_{AR}(\varphi,t)$, can be derived by:

$$T_{emg} = \frac{\partial}{\partial\theta_r}\int_V \frac{B(\varphi,t)^2}{2\mu_0}\mathrm{d}V = \frac{D_o g \ell_{stk}}{4\mu}\frac{\partial}{\partial\theta_r}\int_0^{2\pi}\left[B_{DC}(\varphi,t)+B_{AR}(\varphi,t)\right]^2\mathrm{d}\varphi, \tag{1}$$

where g is the minimum airgap length, μ_0 the vacuum permeability, ℓ_{stk} machine stack length, and D_o is the outer diameter.

The reluctance rotor lacks any active excitation components and consists of a laminated steel core with protrusions, whose number and dimensions are coordinated with the stator characteristics. Both the rotor and stator utilize M19-29G laminated steel. For the design presented in this paper, Fig. 2 illustrates the analyzed minimal region of periodicity, which includes seven rotor protrusions. This section was replicated twice to form the complete cross-section, resulting in 14 rotor protrusions corresponding to 28 magnetic poles.

III. Two-Level Design Optimization

In this section, two-level design optimization as shown by flowchart in Fig. 3, was used to target the maximum power factor, machine goodness, and electromagnetic torque per length in the first level, and minimize the torque ripple in the second level. The 10 independent variables used in the first level of optimization are described in Table I, and shown in Fig. 4. Using a multi-objective differential evolution

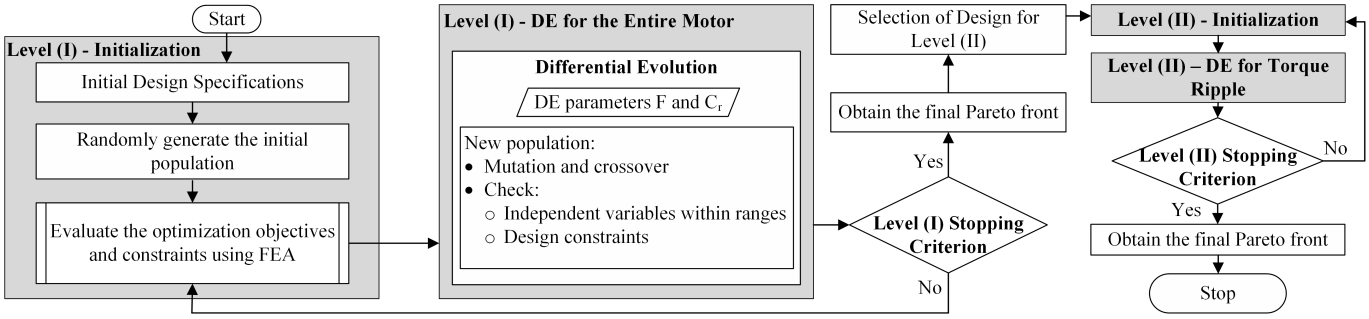

Fig. 3. The flowchart for the proposed two-level optimization algorithm employs the differential evolution (DE) method, and minimizes the effort in achieving a suitable design with many objectives and independent variables.

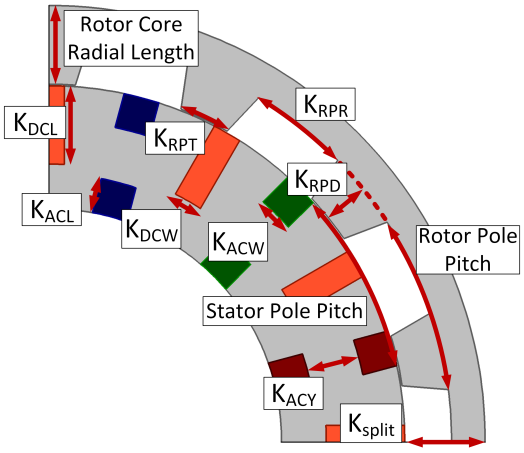

Fig. 4. The independent variables employed for the first level of the optimization process on a quarter of cross-section of the design.

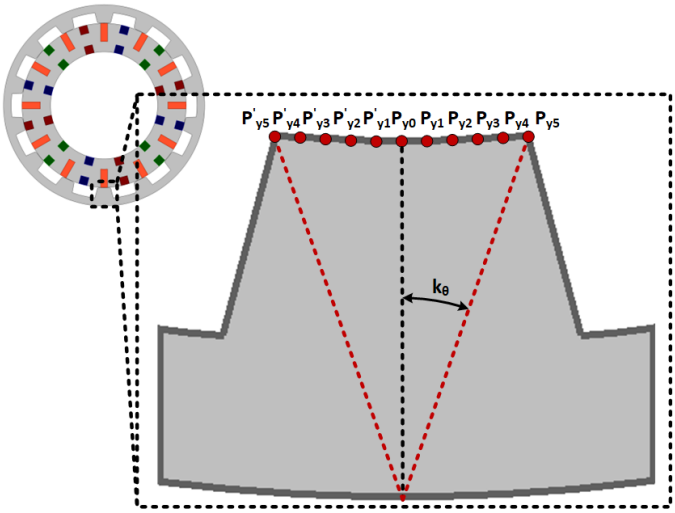

Fig. 5. The independent variables employed for the second level of the optimization process on one of the rotor teeth.

Table I
INDEPENDENT VARIABLES USED FOR THE FIRST LEVEL OF THE OPTIMIZATION, THEIR DESCRIPTION BASED ON DESIGN SPECIFICATIONS, AND CORRESPONDING RANGES.

NO	Variable	Ratios/Descriptions	Min	Max
1	*k_DCL*	DC slot to stator thickness length [–]	0.45	0.55
2	*k_DCW*	DC slot to stator pole width [–]	0.15	0.20
3	*k_ACL*	AC slot to stator thickness length [–]	0.20	0.25
4	*k_ACW*	AC slot to stator pole width [–]	0.15	0.20
5	*k_ACY*	AC yoke to stator thickness length [–]	0.30	0.40
6	*k_RPD*	Rotor pole to rotor core radial length [–]	0.45	0.55
7	*k_RPR*	Rotor pole root to pole pitch [–]	0.45	0.55
8	*k_RPT*	Rotor pole top to pole pitch [–]	0.30	0.70
9	*k_split*	Stator OD/Rotor OD [–]	0.85	0.95
10	airgap	airgap length [mm]	0.90	1.00

(DE) optimization algorithm, which is a popular optimization method and has been implemented in various fields, the design with DC stator excitation introduced in Section II was optimized considering the aforementioned objectives. The selected design as a result of this level is marked on the 3-D Pareto front as shown in Fig. 6.

The design selected from the first level is then employed in the second level of the optimization algorithm with dual objectives: minimizing torque ripple and maximizing torque while maintaining a minimum airgap. The second objective is taken into account to verify that there is no reduction in electromagnetic torque, having a direct correlation with the airgap.

In the second level the optimization algorithm considers the multi-point spline shaping method with 7 independent variables, namely P_{y0}, ..., P_{y5}, and k_θ shown in Fig. 5. The rotor profile was defined by a spline curve, a mathematical representation of an interface for designing and controlling the shape of complex curves. A natural spline, also known as a piece-wise cubic spline, with an end condition ensuring a zero derivative was defined between consecutive points P_i and P_{i+1} as:

$$S_i(x) = a_i + b_i(x - x_i) + c_i(x - x_i)^2 + d_i(x - x_i)^3, \qquad (2)$$

where a_i, b_i, c_i, and d_i represent coefficients determined by specified conditions.

The implementation of the spline is facilitated through Ansys Electronics Desktop software [33], allowing the generation of a poly-line object and the creation of a curve composed of one or more spline segments. This approach enabled the

Table II
INDEPENDENT VARIABLES USED FOR THE SECOND LEVEL OF THE OPTIMIZATION, AND THEIR RANGES FOR A ROBUST DESIGN WITH MINIMUM AIRGAP.

Parameter	Unit	Min.	Max
P_{y0}	[mm]	0	0.2
P_{y1}	[mm]	0	0.3
P_{y2}	[mm]	0	0.4
P_{y3}	[mm]	0.1	0.8
P_{y4}	[mm]	0.2	1.0
P_{y5}	[mm]	0.3	1.5
k_θ	[degree]	6.2	6.6

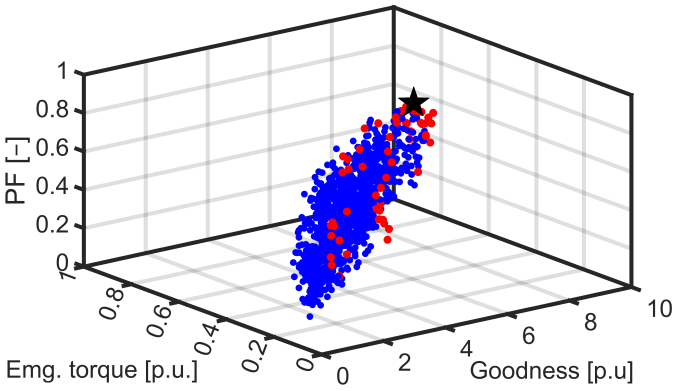

Fig. 6. The normalized results from the first level of optimization aimed at maximizing the machine power factor, torque, and goodness. The selected design is shown with a ★ symbol.

control of the shape of the rotor teeth profile by defining a sequence of points, and the resulting spline closely follows this specified sequence. The implemented multi-point spline shaping for the rotor teeth is depicted in Fig. 5.

IV. RESULTS AND DISCUSSION

The optimization results of the first and second level with the selected design marked, are shown in Figs. 6, and 7, respectively. The electromagnetic torque with unprofiled and

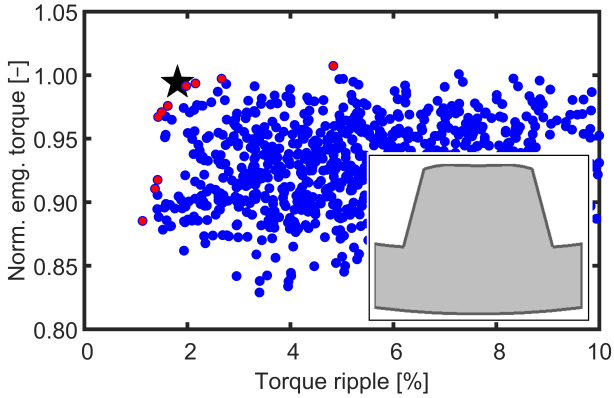

Fig. 7. The second level optimization results showing a minimize torque ripple. The selected design is marked with a ★ symbol. The tooth shape of the selected design is shown.

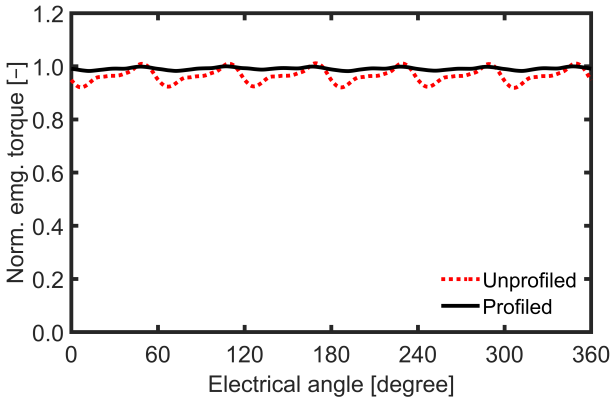

Fig. 8. The electromagnetic torque profile resulting from the second level of optimization exhibits a minimal torque ripple of 2% in the profiled rotor, versus the 10% in the unprofiled rotor.

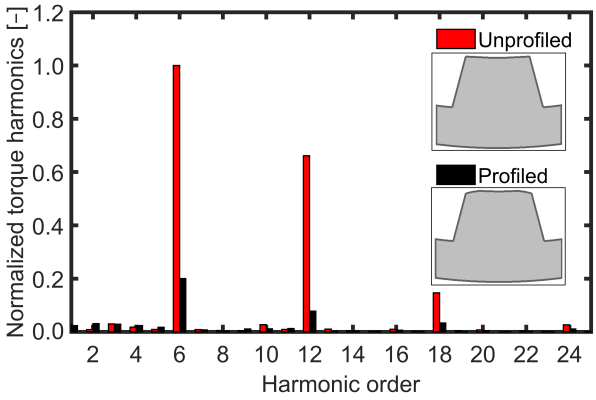

Fig. 9. The harmonic analysis of the electromagnetic torque indicates injection of 6th, 12th, and 18th order harmonics, which contribute to the minimization of torque ripple.

profiled rotor teeth is depicted in Fig. 8, which shows the two-level multi-objective design optimization can successfully *mitigate* the torque ripple by 81% and at the same time *increase* the electromagnetic torque. The harmonic analysis on electromagnetic torque is shown in Fig. 9, where the 6th, 12th, and 18th order harmonics are substantially mitigated, which directly minimized the torque ripple and increased the average electromagnetic torque by 3%.

Further analysis of the design's back-EMF as illustrated in Fig. 10 shows the increase of harmonic content magnitude in the profiled design and therefore accurately computing the force/torque in this design is crucial. Radial and tangential components of the electromagnetic stress in the airgap, denoted as $f_r(\varphi,t)$ and $f_t(\varphi,t)$, respectively, can be expressed using the Maxwell stress tensor method:

$$f_r(\varphi,t) = \frac{B_r(\varphi,t)^2 - B_t(\varphi,t)^2}{\mu_o}, \tag{3}$$

$$f_t(\varphi,t) = \frac{B_r(\varphi,t)B_t(\varphi,t)}{\mu_o}, \tag{4}$$

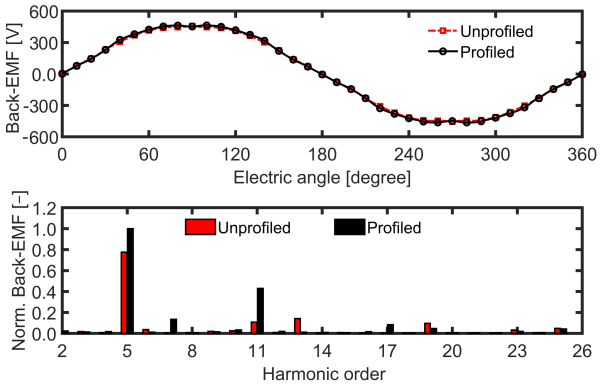

Fig. 10. The open-circuit induced voltage and its normalized harmonic decomposition.

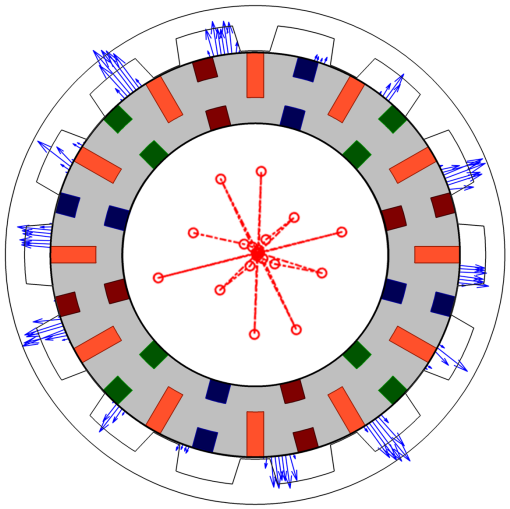

Fig. 11. Electromagnetic forces shown on stator teeth. Blue arrows denote the distributed force vectors and red dots denote the resultant forces on teeth.

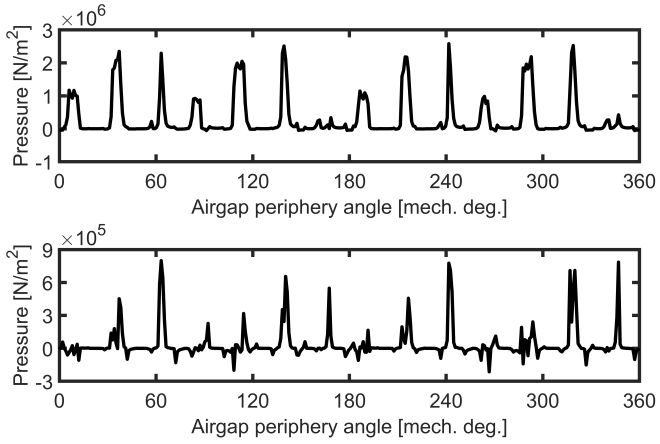

Fig. 12. Airgap stresses at rated load for the profiled rotor. The radial component is shown at the top, and the tangential component is depicted at the bottom.

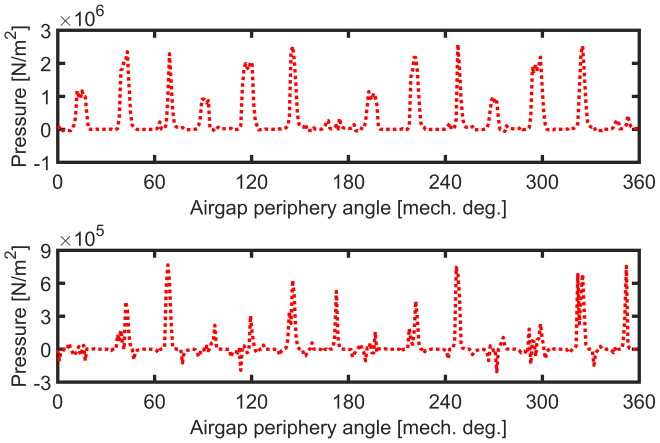

Fig. 13. Airgap stresses at rated load for the unprofiled rotor. The radial component is depicted at the top, and the tangential component is shown at the bottom.

where the radial and tangential airgap flux densities, denoted as $B_r(\varphi, t)$ and $B_t(\varphi, t)$, are calculated using FEA. The radial and tangential forces acting on the stator teeth and rotor protrusions are determined by integrating the corresponding stress components over circumferential intervals, as illustrated in Fig. 11. The analysis results as shown in Figs. 12, and 13 indicate, the radial force density significantly surpasses the tangential components, which is in line with expectations and the ratio of radial to tangential forces is within normal range.

V. Conclusion

The proposed two-level method resulted in a substantial reduction of the torque ripple by 81%, (from 10% down to 2%). The advantages of systematic optimization are also illustrated by the increase in the electromagnetic torque by 3%. The combination of the two stages resulted in a design having also high torque, power factor and overall satisfactory performance, while also reducing the effort required to achieve a suitable design with numerous independent variables. The analysis also compared the Maxwell stress and found that the peak radial and tangential component of the forces have been maintained at the same level as with the unprofiled rotor, so that expected electromagnetic noise is not negatively effected by the rotor teeth profiling.

The novel multi-point spline shaping method, proved to be advantageous in effectively minimizing the machine torque ripple while increasing the electromagnetic torque. This optimization approach, along with the shaping technique, is generally applicable to synchronous machines that includes salient features in the rotor or stator cores. Furthermore, the force analysis and the smooth surface produced by the multi-point spline shaping ensured the design's manufacturability.

Acknowledgment

This paper is based upon research sponsored by QM Power, Inc. The support of ANSYS, Inc., and University of Kentucky the L. Stanley Pigman Chair in Power endowment is also gratefully acknowledged.

REFERENCES

[1] M. Rosu, P. Zhou, D. Lin, D. M. Ionel, M. Popescu, F. Blaabjerg, V. Rallabandi, and D. Staton, *Multiphysics Simulation by Design for Electrical Machines, Power Electronics and Drives*. J. Wiley - IEEE Press, 2017, doi: 10.1002/9781119103462.

[2] H. Ding, Y. Li, S. G. Min, G. Nellis, and B. Sarlioglu, "Design and Evaluation of the Performance of an Integrated Flux-Switching Motor–Compressor With Airfoil-Shaped Rotor," *IEEE Transactions on Transportation Electrification*, vol. 7, no. 3, pp. 1573–1588, 2021.

[3] H. Chen, A. M. EL-Refaie, and N. A. O. Demerdash, "Flux-switching permanent magnet machines: A review of opportunities and challenges—part I: Fundamentals and topologies," *IEEE Transactions on Energy Conversion*, vol. 35, no. 2, pp. 684–698, 2020.

[4] O. A. Badewa, A. Mohammadi, D. M. Ionel, S. Essakiappan, and M. Manjrekar, "Electric vehicle traction motor with a reluctance outer rotor and a modular stator with ac concentrated toroidal windings and pm or dc wave winding excitation," in *2023 IEEE Energy Conversion Congress and Exposition (ECCE)*, 2023, pp. 3845–3850.

[5] M. Abdalmagid, E. Sayed, M. H. Bakr, and A. Emadi, "Geometry and topology optimization of switched reluctance machines: A review," *IEEE Access*, vol. 10, pp. 5141–5170, 2022.

[6] Y. Amara, H. B. Ahmed, and M. Gabsi, *Hybrid Excited Synchronous Machines: Topologies, Design and Analysis*. John Wiley & Sons, 2023, ISBN: 9781786306852.

[7] P. K. Dash and A. K. Das Gupta, "Inductance coefficients of three-phase inductor alternators: Part I - analytical study," *IEEE Transactions on Power Apparatus and Systems*, vol. PAS-88, no. 11, pp. 1725–1730, 1969.

[8] A. Mohammadi, O. A. Badewa, Y. Chulaee, D. M. Ionel, S. Essakiappan, and M. Manjrekar,, "Design Optimization of a Direct-drive Wind Generator with Non-rare-earth PM Flux Intensifying Stator and Reluctance Rotor," in *2023 IEEE International Electric Machines & Drives Conference (IEMDC)*, 2023, pp. 1–6.

[9] C. S. Goli, M. G. Kesgin, P. Han, D. M. Ionel, S. Essakiappan, J. Gafford, and M. D. Manjrekar, "Analysis and design of an electric machine employing a special stator with phase winding modules and pms and a reluctance rotor," *IEEE Access*, vol. 12, pp. 9621–9631, 2024.

[10] A. Mohammadi, O. A. Badewa, Y. Chulaee, D. M. Ionel, S. Essakiappan, and M. Manjrekar, "Direct-Drive Wind Generator Concept with Non-Rare-Earth PM Flux Intensifying Stator and Reluctance Outer Rotor," in *2022 11th International Conference on Renewable Energy Research and Application (ICRERA)*. IEEE, 2022, pp. 582–587.

[11] D. D. Lewis, O. A. Badewa, A. Mohammadi, M. Vatani, and D. M. Ionel, "Fault Tolerant Electric Machine Concept for Aircraft Propulsion with PM Rotor and DC Current Stator Dual-Stage Excitation," in *2023 12th International Conference on Renewable Energy Research and Applications (ICRERA)*, 2023, pp. 607–611.

[12] O. A. Badewa, A. Mohammadi, D. D. Lewis, D. M. Ionel, S. Essakiappan, and M. Manjrekar, "Optimization of an electric vehicle traction motor with a pm flux intensifying stator and a reluctance outer rotor," in *2023 IEEE Transportation Electrification Conference & Expo (ITEC)*, 2023, pp. 1–6.

[13] V. Abramenko, I. Petrov, J. Nerg, and J. Pyrhönen, "Synchronous Reluctance Motors With an Axially Laminated Anisotropic Rotor as an Alternative in High-Speed Applications," *IEEE Access*, vol. 8, pp. 29 149–29 158, 2020.

[14] A. Mohammadi, O. A. Badewa, Y. Chulaee, D. D. Lewis, S. Essakiappan, M. Manjrekar, and D. M. Ionel, "Design Optimization of a Direct-Drive Wind Generator With a Reluctance Rotor and a Flux Intensifying Stator Using Different PM Types," *IEEE Transactions on Industry Applications*, vol. 60, no. 4, pp. 6113–6123, 2024.

[15] A. Bojoi, P. Pescetto, F. Stella, S. Ferrari, and G. Pellegrino, "Direct Flux-and-Torque Vector Control with Active Torque Ripple Minimization," in *2024 IEEE Applied Power Electronics Conference and Exposition (APEC)*, 2024, pp. 1028–1034.

[16] A. Mohammadi, Y. Chulaee, A. M. Cramer, I. G. Boldea, and D. M. Ionel, "Axial Flux Permanent Magnet Vernier Machine with Single-wound Dual-stator and Spoke Permanent Magnet Rotor for Electric Vehicle In-wheel Traction," in *2023 IEEE Transportation Electrification Conference & Expo (ITEC)*, 2023, pp. 1–5.

[17] M. Xu, W. Zhao, J. Ji, Q. Chen, and G. Liu, "Auxiliary Notching Rotor Design to Minimize Torque Ripple for Interior Permanent Magnet Machines," *IEEE Transactions on Industrial Electronics*, vol. 71, no. 10, pp. 12 051–12 062, 2024.

[18] L. R. Huang, J. H. Feng, S. Y. Guo, Y. F. Li, J. X. Shi, and Z. Q. Zhu, "Rotor Shaping Method for Torque Ripple Mitigation in Variable Flux Reluctance Machines," *IEEE Transactions on Energy Conversion*, vol. 33, no. 3, pp. 1579–1589, 2018.

[19] B. Lee, Z. Q. Zhu, and L. R. Huang, "Investigation of torque production and torque ripple reduction method for 6-stator/7-rotor-pole variable flux reluctance machines," in *2017 IEEE Energy Conversion Congress and Exposition (ECCE)*, 2017, pp. 1880–1887.

[20] H.-C. Liu, I.-G. Kim, Y. J. Oh, J. Lee, and S.-C. Go, "Design of Permanent Magnet-Assisted Synchronous Reluctance Motor for Maximized Back-EMF and Torque Ripple Reduction," *IEEE Transactions on Magnetics*, vol. 53, no. 6, pp. 1–4, 2017.

[21] B. Praslicka, D. F. Knight, T. L. Stefanelli, N. Palmer, A. White, J. Jones, and H. A. Toliyat, "Design and Analysis of an Axial Flux Coaxial Magnetic Gear with Balanced Axial Forces for Precision Aerospace Actuation Application," in *2022 IEEE Energy Conversion Congress and Exposition (ECCE)*, 2022, pp. 1–8.

[22] F. Farrokh, H. Torkaman, A. Vahedi, and M. Banejad, "Design of Dual-Rotor Dual-Stator Axial-Field Flux-Switching PM Motor with Low-Cogging Torque and Low-Torque Ripple," in *International Conference on Electrical Machines and Drives (ICEMD)*, 2023, pp. 1–5.

[23] S. E. M. Mohammadi, P. Chen, M. Moallem, B. Fahimi, and M. Kiani, "An Alternate Rotor Geometry for Switched Reluctance Machine With Reduced Torque Ripple," *IEEE Transactions on Energy Conversion*, vol. 38, no. 2, pp. 939–947, 2023.

[24] A. Mohammadi, A. M. Cramer, and D. M. Ionel, "Comparative Analysis of Vernier Machines with Spoke, Surface Mounted, and Halbach PM Rotors for In-wheel Traction," in *2024 IEEE Transportation Electrification Conference & Expo (ITEC)*, 2024, pp. 1–6.

[25] A. Mohammadi, Y. Chulaee, A. M. Cramer, I. G. Boldea, and D. M. Ionel, "Large-scale Design Optimization of an Axial-flux Vernier Machine with Dual Stator and Spoke PM Rotor for EV In-wheel Traction," *IEEE Transactions on Transportation Electrification*, vol. 10, pp. 1–13, 2024.

[26] X. Li, Y. Wang, R. Qu, and N. Bianchi, "Design of Low-Torque-Ripple Permanent Magnet Assisted Synchronous Reluctance Machines with Mirror Asymmetric Rotors," in *IECON 2023- 49th Annual Conference of the IEEE Industrial Electronics Society*, 2023, pp. 1–6.

[27] Z. S. Du and T. A. Lipo, "High Torque Density and Low Torque Ripple Shaped-Magnet Machines Using Sinusoidal Plus Third Harmonic Shaped Magnets," *IEEE Transactions on Industry Applications*, vol. 55, no. 3, pp. 2601–2610, 2019.

[28] Y.-H. Jung, M.-R. Park, and M.-S. Lim, "Asymmetric Rotor Design of IPMSM for Vibration Reduction Under Certain Load Condition," *IEEE Transactions on Energy Conversion*, vol. 35, no. 2, pp. 928–937, 2020.

[29] C. Gan, J. Wu, M. Shen, W. Kong, Y. Hu, and W. Cao, "Investigation of Short Permanent Magnet and Stator Flux Bridge Effects on Cogging Torque Mitigation in FSPM Machines," *IEEE Transactions on Energy Conversion*, vol. 33, no. 2, pp. 845–855, 2018.

[30] H.-C. Liu, I.-G. Kim, Y. J. Oh, J. Lee, and S.-C. Go, "Design of Permanent Magnet-Assisted Synchronous Reluctance Motor for Maximized Back-EMF and Torque Ripple Reduction," *IEEE Transactions on Magnetics*, vol. 53, no. 6, pp. 1–4, 2017.

[31] J. Li, K. Wang, and F. Li, "Reduction of Torque Ripple in Consequent-Pole Permanent Magnet Machines Using Staggered Rotor," *IEEE Transactions on Energy Conversion*, vol. 34, no. 2, pp. 643–651, 2019.

[32] S. Cho, D.-C. Lee, J. Hwang, K. Kim, G. Jang, D.-S. Bae, H. Mok, and C.-W. Kim, "Optimal design to reduce torque ripple of IPM motor with radial based function meta-model considering design sensitivity analysis," *Journal of Mechanical Science and Technology*, vol. 33, pp. 3955–3961, 2019.

[33] Ansys® Electronics Desktop, "Maxwell, version 24.1," 2024, ANSYS, Inc.